Biotribology and biocorrosion of MWCNTs-reinforced PEO coating on AZ31B Mg alloy

Morteza Daavari[*a, b], Masoud Atapour[**a], Marta Mohedano[b], Raul Arrabal[b], Endzhe Matykina[b], Aboozar Taherizadeh[a]

[a] Department of Materials Engineering, Isfahan University of Technology, 84156-83111, Isfahan, Iran

[b] Departamento de Ingeniería Química y de Materiales, Facultad de Ciencias Químicas, Universidad Complutense, 28040, Madrid, Spain

Abstract

Over the last two decades, various methods have been developed for surface modification of Mg alloys among which plasma electrolytic oxidation (PEO) is one of the most effective methods for tailoring surface properties. However, PEO coatings still need to be improved in various aspects, including mechanical and corrosion performances. In the current study, multi-walled carbon nanotubes (MWCNTs) were incorporated into a PEO coating structure via one-step process. Characterization techniques in this study included scanning electron microscopy (SEM), Raman spectroscopy and X-ray diffraction (XRD). Corrosion behavior was evaluated by electrochemical tests taking into account quasi-*in vivo* conditions in order to get closer to implant degradation rates in human body. Dry-wear and tribocorrosion in SBF were also evaluated in reciprocal ball-on-plate mode. According to the findings, MWCNTs induced several microstructural modifications in PEO coating such as formation of ~ 1 μm homogeneous dense barrier layer and irregular-shape porosities. Reinforcement significantly improved pitting corrosion resistance of the PEO coating, yielded a low friction coefficient and decreased wear-related damage by 60%.

* Corresponding Author: morteza.daavari@gmail.com. Phone number: +989171835847
** Co-Corresponding Author: m.atapour@cc.iut.ac.ir

Keywords: Plasma Electrolyte Oxidation (PEO), AZ31B Mg alloy, Multi-walled carbon nanotubes (MWCNTs), Corrosion, Tribocorrosion, Quasi-in vivo.

* Corresponding Author: morteza.daavari@gmail.com. Phone number: +989171835847
** Co-Corresponding Author: m.atapour@cc.iut.ac.ir

1. Introduction

Many researches have been devoted toward investigation of degradable metallic implants during last decades [1]. Owing to the similarity of mechanical, biological and physical properties of Mg and human bone, Mg alloys have become promising candidates for developing degradable implants for load-bearing applications [2, 3]. Despite these desirable properties, Mg alloys often show poor surface performance in terms of corrosion and wear resistance, which can lead to premature mechanical failure and adverse tissue reactions [4].

With the aim to improve these characteristics, different surface modification methods have been investigated during the recent years that can be categorized into the three main groups: (electro)chemical, physical, and mixed (physico-chemical) [5]. Plasma electrolytic oxidation (PEO) is an electrochemical surface treatment for fabricating a hard and adherent coating on valve metals such as magnesium, aluminum, titanium, and their alloys [6, 7]. Many studies have been focused on tuning of PEO process parameters including electrical signal and electrolyte composition in order to optimize the coating properties [8-13]. One of the advantages of PEO processing is easy generation of new phases in coating material, comprised of the substrate and electrolyte constituents; hence, desirable bioactive phases such as forsterite can be achieved using PEO treatment almost by default [14]; whereas extensive efforts are required in order to incorporate the mentioned phase into the surface structure of biomedical implants using other methods [15].

Particles incorporation is an effective approach to enhance one or several properties and add a new functionality to a PEO coating. The effects of incorporation of different particles such as CeO_2, WC, graphene, and graphite on different properties including corrosion, wear and biocompatibility have been recently investigated [16-19]. Multi-walled carbon nanotubes (MWCNT) are biocompatible and high strength nanomaterials that have attracted great interest in the recent years for tissue engineering

[20]. Several studies have reported bridging ability of MWCNTs between cracks tips and stopping cracks propagation [21, 22]. On the other hand, due to their specific structure, carbon nanotubes are able to carry organic compounds such as anti-inflammation drugs and bio-corrosion inhibitors [23, 24]; their cell proliferation stimulation capability, and lubricity features have also been proved in various investigations [25, 26]. Accordingly, carbon nanotubes have the great advantages in comparison to other nano/micro particles such as oxides and graphite.

Incorporation of carbon nanotubes (CNT), single and/or multi-walled, into PEO coatings on Al alloys has been researched in the last decade for wear-resistant industrial applications and demonstrated non-reactive or partially reactive incorporation of CNT with positive results for surface mechanical properties, such as wear resistance. Nevertheless, so far only one work appears to have been attempted in regards to PEO of Mg alloys (Table 1). The scope of existing work concerning MWCNT and Mg/PEO system reveals severe lack of wear and corrosion data related to the Mg/PEO/MWCNTs considering biomedical applications.

In service, elements of orthopedic implants (such as screws and plates) are in contact with each other, living tissues (e.g. bones and muscles) and the physiological environment [33]. Dynamic conditions that take place during surgical manipulations and post-healing period (when fracture immobilization is no longer required) activate a degradation mechanism of failure known as tribocorrosion. On the other hand, wear debris can also provoke certain negative biological response [34, 35]. Thus an ideal biodegradable material for orthopedic implant should have reasonable wear resistance [35]; but as it was also referred before, biomedical Mg alloys suffer from poor wear resistance [4], hence they need to be modified and evaluated before to be used as a real implant.

In summary, MWCNTs are well-known as a multi-functional nanoparticles; they have a great potential to simulateneously promote biological tissue response on one hand and mechanical

(bridging and lubricity effects) surface performance (as demonstrated by composite PEO/MWCNT coatings on Al alloys) on the other hand. Accordingly, incorporation of MWCNTs into PEO coatings on Mg alloys can present multiple advantages for biodegradable orthopaedic implants. Hence, the effects of MWCNTs on the structural and bio-functional features of PEO coatings including bio-corrosion, bio-tribocorrosion and bio-corrosion fatigue deserve to be studied in more depth, especially for orthopedic applications.

In the present research, phosphate-silicate PEO coatings with and without incorporated MWCNT were assessed and compared morphologically, tribologically and electrochemically. It should be noted that in order to simulate the degradation behavior of implants in service, quasi-in vivo conditions have been taken into consideration during corrosion tests. In total, current study can be as a guide for future researches to investigate other aspects of presence of MWCNTs in the PEO coatings microstructure.

2. Materials and methods

2.1. Materials

Wrought AZ31B magnesium alloy (wt.%: 3.1% Al, 0.73% Zn, 0.25% Mn, 0.02% Si, <0.001% Cu, 0.005% Fe, <0.005% Ni, <0.01% Ca, <0.001% Zr, <0.3% others, bal. Mg) supplied by Magnesium Elektron Ltd. was cut into 25 mm × 40 mm × 2.5 mm (for wear and tribocorrosion experiments) and 15 mm × 15 mm × 2.5 mm (for electrochemical tests) size specimens. Prior surface treatment the specimens were ground successively to P1200 grit SiC abrasive paper.

2.2. PEO treatment

PEO treatments were performed for 600 s utilizing an EAC-S2000 power supply (ET system electronic). Following electrical parameters were used to carry out PEO process; square-shape

electrical signal, frequency: 400 Hz, anodic voltage: +405 V, cathodic voltage: -25 V, duty cycle: 50%, initial ramp: 60 s and root mean square (rms) current density limit: 100 mA/cm^2. The electrolyte comprising 10 g/L $Na_3PO_4.12H_2O$, 10 g/L Na_2SiO_3, 1 g/L KOH and 3 g/L CaO (electrolyte pH=13, electrical conductivity=29.7 mS/cm), prepared from deionized water and analytical grade chemicals, was stirred during the PEO process using a magnetic stirrer. Addition of 5 g/L multi-walled carbon nanotubes (MWCNTs) (length: 10-30 μm, outer diameter: 20-30 nm, inner diameter: 5-10 nm – (Figure 1)), supplied by US Research Nanomaterials Inc., was made when required (pH=13, electrical conductivity=30 mS/cm). Due to possible influence of surfactant on the plasma discharge characteristics and coating properties [36], no surfactant was used for dispersing MWCNTs. Furthermore, MWCNTs are dispersed because of having negative zeta potential in alkaline solution [25, 30], therefore a surfactant is not considered necessary; continuous mechanical stirring was sufficient to facilitate dispersion. The coatings were fabricated in a 2 L double jacket glass reactor. In order to maintain the electrolyte temperature close 20 ºC, cooled water was circulated through the mentioned reactor. A cylindrical mesh made of 316 stainless steel was used as a counter electrode. After the PEO process, the coated specimens were rinsed in deionized water and isopropanol and then dried using warm air. The following acronyms were used to identify the specimens: BM (non-coated base material), PEO (PEO-coated) and PCT (PEO with MWCNT) respectively.

2.3. Characterization

JEOL JSM-6400 scanning electron microscope (SEM) equipped with Oxford Link energy-dispersive X-ray (EDS) microanalysis hardware was used to study surface and cross-sectional microstructure of PEO coatings. Presence of MWCNTs in the coatings was confirmed via field emission scanning electron microscopy (FESEM) (SU8000, HITACHI Co.)

Low-angle (1º) X-ray diffraction (XRD) was carried out using a Philips X′pert diffractometer (Cu Kα=1.54056 Å) to investigate the phase composition of the coatings.

The MicroRaman analysis was carried out using a NT-MDT NTEGRA Spectra spectrometer equipped with a Solar TII MS5004i monochromator, a CCD Andor iDUS DU-420 detector (1024 x 128 pixels) and an Olympus modular BX-100 microscope with Olympus MPlanFL 20×/0.45NA objective. A 20 mW solid state laser (filter attenuation 0.1% ND) operated at 532 nm wavelength was used as an excitation source. Grating and acquisition times were 600 l/mm of 300–600 s, respectively.

Surface topography examination of coated and non-coated specimens was carried out using a focus variation optical profilometer InfiniteFocusSL (Alicona, Gmbh, Graz) at different magnifications. High-resolution 3D measurements (10 nm vertical resolution with ×50 objective) over large image fields were carried out using a motorized stage. Surface data was analyzed with IF-Measure Suite software to extract topographic (roughness and wear track depth) information.

2.4. Wear tests

2.4.1. Dry wear

Dry wear tests were carried out to evaluate the coating resistance against possible surface damage resulting from the contact with surgical instruments or other components of the implant. Ball-on-plate wear experiments were done using a linear reciprocating sliding tribometer (Microtest/ MT 60/NI) against an alumina ball (ϕ = 4mm). The normal loads, stroke length and oscillating frequency were 1 and 2 N, 10 mm, and 1 Hz, respectively. Tribometer was set to measure the average coefficient of friction (COF) for every 1000 revolutions. Accordingly, for 500 meters sliding distance, 25 data points were acquired.

2.4.2. Tribocorrosion tests

Tribocorrosion experiments were performed with a normal load of 1 N and a sliding distance of 60 m, all other parameters being the same as in dry wear test. A 200 mL volume of simulated body fluid (SBF) was used as the test environment whose temperature was maintained at 37 ± 0.5 ºC using an IR lamp (Figure 2). SBF solution comprised 8.035 g/L NaCl, 0.355 g/L $NaHCO_3$, 0.225 g/L KCl, 0.231 g/L $K_2HPO_4.3H_2O$, 0.311 g/L $MgCl_2.6H_2O$, and 0.292 g/L $CaCl_2$, 0.072 Na_2SO_4 (pH = 7.4) [37]. Open circuit potential (OCP) was measured using an ACM instruments GillAC computer-controlled potentiostat and Ag/AgCl reference electrode before, during and after the sliding period (commencing 30 min before and finishing 30 min after the sliding period). The tests were repeated as necessary (up to three times) to achieve reproducibility.

2.4.3. Electrochemical measurements

Potentiodynamic polarization experiments were done using an ACM instruments GillAC computer-controlled potentiostat and conventional three-electrode system. Graphite and silver/silver chloride (Ag/AgCl, 3 M KCl) electrodes were utilized as the counter and reference electrodes, respectively. The working electrode was the test material and the solution was SBF. The polarization curves were obtained after 0.5 h and 50 hours of immersion at a scan rate of 0.167 mV/s from -200 mV to +1000 mV with respect to the OCP.

In order to simulate the human body environment, a special setup (Figure 3) was designed that controlled simultaneously the temperature, pH and fluid flow rate. A pH controller module (Pro Flora JBL) connected to a CO_2 gas cylinder was utilized to maintain the pH at 7.4±0.1. A Thermostat (Bunsen/TFB and MC-8) was used to maintain the temperature of the double jacket corrosion cell at 37±0.5 ºC during the test. Furthermore, in order to circulate SBF with a proper flow rate (2

ml/min/100 ml) [38], a continuous dripping system was used. The SBF was injected into the corrosion cell using a hypodermic needle.

3. Results and discussion

3.1. Current/Voltage -time response for PEO treatment

Current/voltage-time responses corresponding to the PEO and PCT coatings are presented in Figure 4. The responses can be divided into two main stages. During the first stage (up to ~125 s), the current density reaches the limiting value of 100 mA/cm^2; the fact that it is maintained means that the set voltage amplitude (+405/-25 V) has not been reached. At the beginning of the second stage (~125 - 600 s), a current drop is observed, i.e. the current density decreases by ~75% to ~25 mA/cm^2. This behavior is a common feature under voltage-controlled mode; once the coating impedance and consequently the resistance of the oxide material to mass transfer become sufficiently high, the current drop should happen in order to satisfy the Ohm's law in accordance with the set voltage amplitude [39]. It should be noted that because of the insolubility of CaO and subsequent low transparency of the electrolyte clear observation of the micro-discharges was not possible. However, judging by the acoustic emission, the micro-discharges continued during the second stage, although with much lesser intensity. Therefore, the second stage is expected to increase the coating compactness rather than to contribute to the coating thickness.

The addition of the multi-walled carbon nanotubes caused two notable effects. Firstly, the current-time curve for PEO shows a large peak at ~60-90 s that exceeds the set current limit. This means that intense micro-discharges (of B-type) [40] penetrating the entire coating are taking place and the power supply is not coping with the sudden loss of resistance, hence the current surge. The fact that this peak lasts several tens of seconds suggests that a cascade of discharges is most likely occurring

recurrently at defective sites despite the extinguishing effect of negative pulses. However, in case of the PCT, this peak is not observed, suggesting that the higher thermal conductivity of the electrolyte containing MWCNTs leads to faster cooling of the electrolyte at the end of the plasma column, attenuating the duration and temperature of the micro-discharges, thus inhibiting reiterative cascades and coating damage [41, 42].

The second effect concerns with dielectric breakdown voltage: the PCT coating dielectric breakdown voltage (235 V) is slightly higher than dielectric breakdown voltage corresponding to the PEO coating (220 V). Mentioned difference can be related to higher heat dissipation in PCT coating leads to lower heat accumulation, therefore the film can grow a bit thicker before it breaks, whereas the PEO coating experiences earlier dielectric breakdown [43].

3.2. Coatings characteristics

Macroscopic appearances of the PEO and PCT coatings captured with optical profilometer are depicted in Figure 5 (a) and (b) respectively. As it can be seen, there is a clear color difference between PEO and PCT coatings. In order to quantitate this difference, CMYK (cyan-magenta-yellow key) criteria were used. Accordingly, PEO coating contains 9.4% of black agent, while PCT coating has 78.1% of it. This significant difference is likely the result of the incorporation of MWCNTs into the oxide layer. In order to confirm this, other characterization methods were also employed in the present study.

Figure 5 (c, d, e, and f) shows the optical profilometry images of PEO and PCT coatings. Roughness values (R_a and R_z) for PEO and PCT coatings are (0.281±0.025) / (1.395±0.189) μm and (0.442±0.047) / (1.99±0.324) μm, respectively. This means that PCT coating has a rougher surface than PEO coating. As shown in Figure 6 (a) and (b), this rougher surface is related to the formation

of bigger pores in the presence of MWCNTs. This is likely related to (i) the higher thermal conductivity of the MWCNTs-containing electrolyte promoting faster cooling rates after each discharge is extinguished and (ii) oxidation of MWCNTs and the resultant evolution of additional gas (CO and CO_2). By contrast, the MWCNTs-free electrolyte produces a characteristic smooth volcano-like morphology [44], which is indicative of a longer time given to the molten coating material to flow and fill up the pores and other coating defects before its solidification.

Coating porosity can provide an appropriate space for cell adhesion and proliferation and increase coating biocompatibility [45], porosity percentages of PEO and PCT coatings were analyzed using ImageJ software. According to the Figure 6 (a-inset) and (b-inset), porosity percentages corresponding to the PEO and PCT coatings are 4.31% and 15.89% respectively. This implies higher porosity-related biocompatibility of PCT coating in comparison to PEO coating. Furthermore, PCT coating establish a better under layer for a possible duplex treatment.

Figure 7 (a and b) depict the high magnification FE-SEM micrographs of PCT and PEO coatings, respectively. As illustrated, MWCNTs have been embedded into the superficial layers of PCT coating. On the other hand, there are some long cracks in PEO coating, typical of thermal contraction, which are probably the result of the intense discharges occurring during the early stages of the treatment (according to the discussion in section 3.1). It worth to be noted that, presence of MWCNTs on the surface structure of PCT coating establishes the idea of drug loading into the MWCNTs via a soaking period as a post surface treatment.

The results of EDS area analyses of PEO and PCT coatings are presented in Table 2. Based on the EDS spectra, both coatings are mainly consisting of magnesium, oxygen, silicon, phosphorous and small amounts of calcium and aluminum. All except Mg and Al are incorporated from the electrolyte. Mg and Al come from the substrate and aluminum-manganese-iron intermetallic particles

present in the substrate matrix, respectively [46]. Comparison of the percentage of carbon content related to PEO and PCT can clearly reveal that MWCNTs has incorporated into oxide layer successfully; the presence of ~10.8at.% of carbon in PEO coatings possibly results from surface contamination with organic substances and CO_2 adsorption.

Figure 6 (c) and (d) depict the polished cross-section SEM micrographs of PCT and PEO coated samples, respectively. The coating thickness measurements show an increase from ~7.5 μm to ~10 μm following the incorporation of MWCNTs into the coating. Additionally, MWCNTs cause the increase in the number and the size of pores. Another notable difference between PEO and PCT coatings is the formation of the relatively thick (~1μm) dense barrier layer for PCT coating, while the barrier layer of PEO coating appears less homogeneous.

In order to make sure that MWCNTs got incorporated into the PEO coating, Raman measurements were also conducted. Figure 8 compares the Raman spectra of MWCNTs powders, PEO and PCT coatings. The Raman spectrum of MWCNTs exhibits a peaks at ~1343 cm^{-1} (D band, attributed to amorphous carbon and structural defects); ~1568 cm^{-1} (G band, originated from tangential vibrations of carbon atoms in the graphite structure); and at ~2679cm^{-1} (G′ band, associated with the long range graphite ordering). As expected, in contrary to Raman spectrum of PEO, Raman spectrum of PCT poses three peaks at ~1346 cm^{-1} (D band), ~1583 cm^{-1} (G band), and ~2694 cm^{-1} (G′ band), which supports the FE-SEM observations and EDS analyses and, subsequently, confirms the incorporation of MWCNTs into the coating. It is worth to mention the higher intensity of the D band for the PCT coating compared to that of MWCNTs powder, which indicates a higher amount of amorphous carbon in PCT coating [47], which indicates that MWCNTs undergo a certain level of degradation under plasma micro-discharge.

In accordance with XRD patterns obtained from PEO and PCT coatings (Figure 9), PEO coating consists of MgO crystalline phase. Magnesium peaks were also detected because of the reaching of X-rays to the magnesium substrate. PCT coating consists of Mg_2SiO_4 crystalline phase in addition to MgO.

Based on the previously published literature, energy input plays a determining role in the chemical composition of formed crystalline phases; accordingly, in order to incorporate electrolyte components into the final coating, a certain energy level is required [48]. Regarding the XRD and EDS results, there is a clear difference between the two coatings, manifested as the existence of Si- and P-rich amorphous phase in the PEO coating and crystalline Mg_2SiO_4 in PCT coating. Furthermore, phosphorous content in PEO coating is over five times greater than that in PCT. Greater incorporation of both Si and P in case of PEO coating can be related to longer lasting micro-discharges (as the current surge above the set limit suggests, Figure 4). Phosphorous, in particular, is known to promote formation of amorphous coating material in PEO coatings [49], hence the lack of crystalline Mg_2SiO_4 in PEO coating.

3.3. Performance evaluation

3.3.1. Dry wear

Figure 10 reveals the variations of coefficients of friction (COF) with sliding distance (500 m) for Mg alloy substrate (BM), PEO and PCT coatings under the atmospheric condition. As illustrated, COF of the substrate keeps increasing with the sliding distance. This could be related to increasing surface roughness due to local plastic deformation (e.g. ploughing effect) and to the production of wear debris, e.g. hard Al-Mn-Fe intermetallic particles, activating mechanisms such as three bodies abrasive wear (debris effect) [50] (Figure 11 (a and b)).

The PEO coating shows almost an identical behavior as BM with a slightly lower slope. Regarding to the Figure 11 (c, d, e, f and g), PEO and PCT coatings yield about two hundred times lower wear track depth, which must be attributed to a much lesser debris effect and negligible ploughing due to strain hardening; therefore, the obtained behavior is expectable and in agreement with previous studies [51, 52].

The tribological behavior of PCT coating is completely different from the other studied specimens. In spite of higher initial value, COF of PCT coating has experienced a slight decrement with sliding distance and for the greater part of the experiment remained ~15% lower than that of PEO coating. It can be deduced that in addition to strain hardening and debris, an additional factor is involved in wear mechanism of PCT coating: abrasion of the superficial layers of PCT coating uncovers the embedded MWCNTs, which provide a lubricant effect [28].

In order to assess and compare the wear resistance (considering as a failure the moment when alumina ball reached the substrate) of PEO and PCT coatings against higher load (2 N, 50 m), a statistical study was also carried out. Accordingly, PCT coating has passed all 12 dry wear experiments successfully, while PEO coating failed in 6 experiments out of 12 before 25 m of sliding distance.

3.3.2. Tribocorrosion

As mentioned in the experimental section, tribocorrosion experiments were performed to simulate the in-vivo wear-related damage. It is worth noting that SBF plays two contradictory roles during tribocorrosion testing. It acts as a lubricant, thus reducing the coefficient of friction and the likelihood of wear (lubricity effect), but, at the same time, is a corrosive medium (destructive effect) [52]. According to the results presented in Figure 11 (g), wear track depth of BM after tribocorrosion test is less than 50% of that of dry wear test; it means that lubricity effect is the dominant effect for

BM. By contrast, the destructive effect of SBF is more evident for PEO and PCT coatings, when comparing with the corresponding dry wear test. Nevertheless, the protective effect of PEO and PCT coatings against tribocorrosion is evident when comparing with BM, as they yield about 20 times more shallow wear tracks.

Figure 12 shows the measurement of the open circuit potential (OCP) before, during and after the tribocorrosion experiments. During the first 30 min, the OCP of the uncoated specimen increased from ~-1675 $mV_{Ag/AgCl}$ up to ~-1575 $mV_{Ag/AgCl}$, which is attributed to surface passivation. Then, during the sliding period, the passive layer is destroyed and OCP drops to relatively stable values (-1650 $mV_{Ag/AgCl}$). As soon as the sliding period ends, the passivation layer starts to regrow and OCP increases accordingly. Other researchers [53] have reported similar observations.

The PEO coating shows a similar trend. In this case, the OCP evolution can be interpreted as follows:

1) Coating hydration. The increased volume of phases such as MgO due to hydration causes a deterioration of the coating cohesion/adhesion strength [54].

2) Removal of loose coating material. EDS analyses inside and at the vicinity of the wear track (Figure 13) revealed significant differences in the content of magnesium (53.44at.% vs. 17.89at.%), oxygen (22.65at.% vs. 1.82 at.%) and silicon (0.13 at.% vs. 6.22at.%). These findings show that, during sliding period, the PEO coating has worn out and the alumina ball has come in direct contact with the substrate.

3) Repassivation of the wear track. This stage resembles that of the base material. A passive layer forms at the bottom of the wear track, that is why the wear depth (~ 2.95 μm) measured at the end of the experiment is possibly lower than the one formed at the end of the sliding period.

These findings and interpretation are in agreement with other tribological studies of phosphate and silicate-based PEO coatings on a Mg-Al-Zn alloy [53].

For PCT coating, the average value of OCP was relatively constant during the tribocorrosion test before, during and after the sliding period. In addition, the chemical compositions determined inside and outside of the wear track were relatively similar. These features (the OCP value and trend and chemical composition) are completely different from those observed in BM and PEO coating. The improved corrosion/wear behavior of the PCT coating is attributed to two factors: the presence of Mg_2SiO_4 in the coating, which is less prone to hydrolysis than the MgO and amorphous phases found in the PEO coating, and the improved lubricity due to the presence of MWCNTs and amorphous carbon [55].

3.4. Potentiodynamic Polarization

Potentiodynamic polarization curves of BM, PEO, and PCT specimens for two different immersion times (0.5 h and 50 h) in SBF are presented in Figure 14. The electrochemical parameters (corrosion potential, corrosion current density, and pitting potential) are summarized in Table 3. The corrosion potential of BM has become nobler with immersion time because of the formation and growth of passive layer, although its corrosion rate increased [56]. PEO and PCT coatings did not reveal a significant effect on the corrosion potential (E_{corr}), whereas the corrosion current density (i_{corr}) was reduced by 3 orders of magnitude in comparison with the base material. This shows that the coatings act as barrier layers that delay the ingress of corrosive species towards the substrate. However, this barrier effect significantly diminishes for the PEO coating after 50 h of immersion. As it can be seen in Figure 14 and Table 3, PCT coating still provides protection after 50 h. Based on what has been reported in previous studies, PEO coatings on Mg typically exhibit two layers with the dense inner layer playing the most important role from the point of view of corrosion protection [57]. Therefore, the superior corrosion performance of the PCT coating could be explained by its homogeneous dense inner layer and impeded hydration due to the presence of Mg_2SiO_4 in its composition.

Pitting corrosion is one of the most important forms of corrosion in biomedical implants; corrosion pits reduce the load bearing capacity and are potential nucleation sites for cracking [58]. The pitting potential or breakdown potential (E_{bd}) reflects the susceptibility of an alloy to localized corrosion. As it can be seen from polarization plots (Figure 14), the interval $E_{bd} - E_{corr}$ corresponding to PEO and PCT coatings are 30 mV and 80 mV, respectively, after 0.5h immersion. This implies that PCT coating exhibits superior pitting corrosion resistance. After 50 h immersion, PEO coating loses its resistance due to pitting corrosion as E_{bd} and E_{corr} coincide and no passivation is observed. By contrast, pitting corrosion resistance of PCT coating further improves after 50 h immersion; as MWCNTs were detected by Raman inside the pores of PCT coating (Figure 15), this is believed to be associated with the mechanical reinforcing characteristics of MWCNTs within the coating, thereby delaying the loss of coating adhesion/cohesion [59]. The ability of MWCNTs to entrap Cl^- ions that has been reported by Dalla et al [60] may also play a role in improved pitting corrosion resistance.

4. Conclusions

The following conclusions can be derived from the above results and discussion:

- Successful incorporation of MWCNTs into the microstructure of oxide coating was carried out via one step PEO process.
- Incorporation of MWCNTs induced bigger size pores, uniformly thick and dense barrier layer and formation of Mg_2SiO_4 in addition to MgO in comparison to MWCNT-free coating.
- MWCNTs enhanced dry wear performance of PCT coating by reducing the coefficient of friction by 15% and wear depth by 60% in comparison to MWCNT-free coating.

- MWCNTs provided a stable tribocorrosion performance of PCT coating uncompromised by decrease of corrosion potential attributed to coating's improved lubricity and resistance to hydration.
- Overall better corrosion resistance of PCT coating compared to PEO coating during quasi-*in vivo* electrochemical polarization is due to a dense uniform barrier layer and impeded hydration of the crystalline phases in the coating.
- MWCNT reinforcement inside the pores of the PCT coating provides enhanced pitting corrosion resistance compared to reinforcement-free coating due to delayed loss of coating adhesion/cohesion.

Acknowledgements

The authors gratefully acknowledge the financial support of the Iran National Science Foundation INSF (Grant No. 97014179). This work was also supported by RTI2018-096391-B-C33 (MCIU/AEI/FEDER, UE) and S2018/NMT-4411 (Regional government of Madrid and EU Structural and Social Funds). M. Mohedano is grateful for the support of RYC-2017-21843.

References

[1] Chagnon, M., Guy, L. G., & Jackson, N. (2019). Evaluation of Magnesium-based Medical Devices in Preclinical Studies: Challenges and Points to Consider. *Toxicologic pathology*, *47*(3), 390-400.

[2] Yang, H., Jia, B., Zhang, Z., Qu, X., Li, G., Lin, W., ... & Zheng, Y. (2020). Alloying design of biodegradable zinc as promising bone implants for load-bearing applications. *Nature communications*, *11*(1), 1-16.

[3] Zhang, C., Lin, J., Nguyen, N. Y. T., Guo, Y., Xu, C., Seo, C., ... & Liu, H. (2019). Antimicrobial Bioresorbable Mg–Zn–Ca Alloy for Bone Repair in a Comparison Study with Mg–Zn–Sr Alloy and Pure Mg. *ACS Biomaterials Science & Engineering*, *6*(1), 517-538.

[4] Song, G., & StJohn, D. (2002). The effect of zirconium grain refinement on the corrosion behaviour of magnesium-rare earth alloy MEZ. *Journal of Light Metals*, *2*(1), 1-16.

[5] Narayanan, T. S., Park, I. S., & Lee, M. H. (2015). Surface modification of magnesium and its alloys for biomedical applications: opportunities and challenges. In *Surface Modification of Magnesium and its Alloys for Biomedical Applications* (pp. 29-87). Woodhead Publishing.

[6] Rahmati, M., Raeissi, K., Toroghinejad, M. R., Hakimizad, A., & Santamaria, M. (2019). Effect of pulse current mode on microstructure, composition and corrosion performance of the coatings produced by plasma electrolytic oxidation on AZ31 Mg alloy. *Coatings*, *9*(10), 688.

[7] Matykina, E., Garcia, I., Arrabal, R., Mohedano, M., Mingo, B., Sancho, J., ... & Pardo, A. (2016). Role of PEO coatings in long-term biodegradation of a Mg alloy. *Applied Surface Science*, *389*, 810-823.

[8] Chang, L., Tian, L., Liu, W., & Duan, X. (2013). Formation of dicalcium phosphate dihydrate on magnesium alloy by micro-arc oxidation coupled with hydrothermal treatment. *Corrosion science*, *72*, 118-124.

[9] Gu, Y., Chen, C. F., Bandopadhyay, S., Ning, C., Zhang, Y., & Guo, Y. (2012). Corrosion mechanism and model of pulsed DC microarc oxidation treated AZ31 alloy in simulated body fluid. *Applied surface science*, *258*(16), 6116-6126.

[10] Guo, H. F., An, M. Z., Huo, H. B., Xu, S., & Wu, L. J. (2006). Microstructure characteristic of ceramic coatings fabricated on magnesium alloys by micro-arc oxidation in alkaline silicate solutions. *Applied surface science*, *252*(22), 7911-7916.

[11] Lee, Y. K., Lee, K., & Jung, T. (2008). Study on microarc oxidation of AZ31B magnesium alloy in alkaline metal silicate solution. *Electrochemistry communications*,

10(11), 1716-1719.

[12] Kim, D. J., Kim, M. J., Kim, J. S., & Kim, H. P. (2008). Material characteristics of Ni–P–B electrodeposits obtained from a sulfamate solution. *Surface and Coatings Technology*, *202*(12), 2519-2526.

[13] Yan, G., Guixiang, W., Guojun, D., Fan, G., Lili, Z., & Milin, Z. (2008). Corrosion resistance of anodized AZ31 Mg alloy in borate solution containing titania sol. *Journal of alloys and compounds*, *463*(1-2), 458-461.

[14] Wang, Y., Chen, M., & Zhao, Y. (2019). Preparation and Corrosion Resistance of Microarc Oxidation-Coated Biomedical Mg–Zn–Ca Alloy in the Silicon–Phosphorus-Mixed Electrolyte. *ACS omega*, *4*(25), 20937-20947.

[15] Prakash, P. S., Pawar, S. J., & Tewari, R. P. (2019). Synthesis, characterization, and coating of forsterite (Mg_2SiO_4) based material over medical implants: A review. *Proceedings of the Institution of Mechanical Engineers, Part L: Journal of Materials: Design and Applications*, *233*(6), 1227-1240.

[16] Liu, W., Liu, Y., Lin, Y., Zhang, Z., Feng, S., Talha, M., ... & Shi, T. (2019). Effects of graphene on structure and corrosion resistance of plasma electrolytic oxidation coatings formed on D16T Al alloy. *Applied Surface Science*, *475*, 645-659.

[17] NasiriVatan, H., Ebrahimi-Kahrizsangi, R., & Asgarani, M. K. (2016). Tribological performance of PEO-WC nanocomposite coating on Mg alloys deposited by plasma electrolytic oxidation. *Tribology International*, *98*, 253-260.

[18] Atapour, M., Blawert, C., & Zheludkevich, M. L. (2019). The wear characteristics of CeO_2 containing nanocomposite coating made by aluminate-based PEO on AM50 magnesium alloy. *Surface and Coatings Technology*, *357*, 626-637.

[19] Yin, B., Peng, Z., Liang, J., Jin, K., Zhu, S., Yang, J., & Qiao, Z. (2016). Tribological behavior and mechanism of self-lubricating wear-resistant composite coatings fabricated by one-step plasma electrolytic oxidation. *Tribology International*, *97*, 97-107.

[20] Pei, B., Wang, W., Dunne, N., & Li, X. (2019). Applications of Carbon Nanotubes in Bone Tissue Regeneration and Engineering: Superiority, Concerns, Current Advancements, and Prospects. *Nanomaterials*, *9*(10), 1501.

[21] Ormsby, R., McNally, T., Mitchell, C., & Dunne, N. (2010). Influence of multiwall carbon nanotube functionality and loading on mechanical properties of PMMA/MWCNT bone cements. *Journal of Materials Science: Materials in Medicine*, *21*(8), 2287-2292.

[22] Naqi, A., Abbas, N., Zahra, N., Hussain, A., & Shabbir, S. Q. (2019). Effect of multi-walled carbon nanotubes (MWCNTs) on the strength development of cementitious

materials. *Journal of Materials Research and Technology*, *8*(1), 1203-1211.

[23] Luo, X., Matranga, C., Tan, S., Alba, N., & Cui, X. T. (2011). Carbon nanotube nanoreservior for controlled release of anti-inflammatory dexamethasone. *Biomaterials*, *32*(26), 6316-6323.

[24] Farag, A. A. (2020). Applications of nanomaterials in corrosion protection coatings and inhibitors. *Corrosion Reviews*, *38*(1), 67-86.

[25] Tripathi, P., Katiyar, P. K., Ramkumar, J., & Balani, K. (2020). Synergistic role of carbon nanotube and yttria stabilised zirconia reinforcement on wear and corrosion resistance of Cr-based nano-composite coatings. *Surface and Coatings Technology*, *385*, 125381.

[26] Koumoulos, E. P., & Charitidis, C. A. (2017). Lubricity assessment, wear and friction of CNT-based structures in nanoscale. *Lubricants*, *5*(2), 18.

[27] Lee, K. M., Ko, Y. G., & Shin, D. H. (2011). Incorporation of multi-walled carbon nanotubes into the oxide layer on a 7075 Al alloy coated by plasma electrolytic oxidation: Coating structure and corrosion properties. *Current Applied Physics*, *11*(4), S55-S59.

[28] Lee, K. M., Jo, J. O., Lee, E. S., Yoo, B., & Shin, D. H. (2011). Incorporation of carbon nanotubes into oxide layer on 7075 Al alloy by plasma electrolytic oxidation. *Journal of the Electrochemical Society*, *158*(10), C325.

[29] Yazıcı, S. K., Muhaffel, F., & Baydogan, M. (2014). Effect of incorporating carbon nanotubes into electrolyte on surface morphology of micro arc oxidized Cp-Ti. *Applied surface science*, *318*, 10-14.

[30] Yürektürk, Y., Muhaffel, F., & Baydoğan, M. (2015). Characterization of micro arc oxidized 6082 aluminum alloy in an electrolyte containing carbon nanotubes. *Surface and Coatings Technology*, *269*, 83-90.

[31] Sabouri, M., & Khoei, S. M. (2018). Plasma electrolytic oxidation in the presence of multiwall carbon nanotubes on aluminum substrate: morphological and corrosion studies. *Surface and Coatings Technology*, *334*, 543-555.

[32] Hwang, M., & Chung, W. (2018). Effects of a carbon nanotube additive on the corrosion-resistance and heat-dissipation properties of plasma electrolytic oxidation on AZ31 magnesium alloy. *Materials*, *11*(12), 2438.

[33] Živić, F., Grujović, N., Manivasagam, G., Richards, C., Landoulsi, J., & Petrović, V. (2014). The Potential of Magnesium Alloys as Bioabsorbable/Biodegradable Implants

for Biomedical Applications. *Tribology in Industry*, *36*(1).

[34] Azzi, M., & Klemberg-Sapieha, J. E. (2011). Tribocorrosion test protocols for sliding contacts. In *Tribocorrosion of Passive Metals and Coatings* (pp. 222-238). Woodhead Publishing.

[35] Kumar, K., Gill, R. S., & Batra, U. (2018). Challenges and opportunities for biodegradable magnesium alloy implants. *Materials technology*, *33*(2), 153-172.

[36] Li, Q., Liang, J., & Wang, Q. (2013). Plasma electrolytic oxidation coatings on lightweight metals. *Modern surface engineering treatments*, *4*, 75.

[37] Kokubo, T. (1991). Bioactive glass ceramics: properties and applications. *Biomaterials*, *12*(2), 155-163.

[38] Duan, Y. R., Yao, Z., Wang, C. Y., Chen, J. Y., & Zhang, X. D. (2002). A study of bone-like apatite formation on porous calcium phosphate ceramics in dynamic SBF. *Sheng wu yi xue gong cheng xue za zhi= Journal of biomedical engineering= Shengwu yixue gongchengxue zazhi*, *19*(3), 365.

[39] Matykina, E., Arrabal, R., Pardo, A., Mohedano, M., Mingo, B., Rodríguez, I., & González, J. (2014). Energy-efficient PEO process of aluminium alloys. *Materials Letters*, *127*, 13-16.

[40] Hussein, R. O., Northwood, D. O., & Nie, X. (2010). Coating growth behavior during the plasma electrolytic oxidation process. *Journal of Vacuum Science & Technology A: Vacuum, Surfaces, and Films*, *28*(4), 766-773.

[41] Dunleavy, C. S., Golosnoy, I. O., Curran, J. A., & Clyne, T. W. (2009). Characterisation of discharge events during plasma electrolytic oxidation. *Surface and Coatings Technology*, *203*(22), 3410-3419.

[42] Moghaddari, M., Yousefi, F., Aparicio, S., & Hosseini, S. M. (2020). Thermal conductivity and structuring of multiwalled carbon nanotubes based nanofluids. *Journal of Molecular Liquids*, 112977.

[43] Albella, J. M., Montero, I., Martinez-Duart, J. M., & Parkhutik, V. (1991). Dielectric breakdown processes in anodic Ta_2O_5 and related oxides. *Journal of materials science*, *26*(13), 3422-3432.

[44] Yerokhin, A. L., Nie, X., Leyland, A., Matthews, A., & Dowey, S. J. (1999). Plasma electrolysis for surface engineering. *Surface and coatings technology*, *122*(2-3), 73-93.

[45] Yazdimamaghani, M., Razavi, M., Vashaee, D., Moharamzadeh, K., Boccaccini, A. R., & Tayebi, L. (2017). Porous magnesium-based scaffolds for tissue engineering.

Materials Science and Engineering: C, *71*, 1253-1266.

[46] Bland, L. G., Fitz-Gerald, J. M., & Scully, J. R. (2016). Metallurgical and electrochemical characterization of the corrosion of AZ31B-H24 tungsten inert gas weld: isolated weld zones. *Corrosion*, *72*(9), 1116-1132.

[47] Lehman, J. H., Terrones, M., Mansfield, E., Hurst, K. E., & Meunier, V. (2011). Evaluating the characteristics of multiwall carbon nanotubes. *Carbon*, *49*(8), 2581-2602.

[48] Blawert, C., Sah, S. P., Scharnagl, N., & Kannan, M. B. (2015). Plasma electrolytic oxidation/micro-arc oxidation of magnesium and its alloys. In *Surface modification of magnesium and its alloys for biomedical applications* (pp. 193-234). Woodhead Publishing.

[49] Matykina, E., Monfort, F., Berkani, A., Skeldon, P., Thompson, G. E., & Gough, J. (2007). Characterization of spark-anodized titanium for biomedical applications. *Journal of The Electrochemical Society*, *154*(6), C279.

[50] Sun, H. Q., Shi, Y. N., & Zhang, M. X. (2008). Wear behaviour of AZ91D magnesium alloy with a nanocrystalline surface layer. *Surface and Coatings Technology*, *202*(13), 2859-2864.

[51] Hussein, R. O., Nie, X., & Northwood, D. O. (2017). Plasma electrolytic oxidation coatings on Mg alloys for improved wear and corrosion resistance. *Corrosion: Material Performance and Cathodic Protection*, *99*, 133-134.

[52] Dai, J., Zhang, X., Yin, Q., Ni, S., Ba, Z., & Wang, Z. (2017). Friction and wear behaviors of biodegradable Mg-6Gd-0.5 Zn-0.4 Zr alloy under simulated body fluid condition. *Journal of magnesium and alloys*, *5*(4), 448-453.

[53] Pezzato, L., Vranescu, D., Sinico, M., Gennari, C., Settimi, A. G., Pranovi, P., ... & Dabalà, M. (2018). Tribocorrosion properties of PEO coatings produced on AZ91 magnesium alloy with silicate-or phosphate-based electrolytes. *Coatings*, *8*(6), 202.

[54] Arrabal, R., Mota, J. M., Criado, A., Pardo, A., Mohedano, M., & Matykina, E. (2012). Assessment of duplex coating combining plasma electrolytic oxidation and polymer layer on AZ31 magnesium alloy. *Surface and Coatings Technology*, *206*(22), 4692-4703.

[55] Srinivasan, P. B., Liang, J., Blawert, C., Störmer, M., & Dietzel, W. (2009). Effect of current density on the microstructure and corrosion behavior of plasma electrolytic oxidation treated AM50 magnesium alloy. *Applied Surface Science*, *255*(7), 4212-4218.

[56] Chelliah, N. M., Padaikathan, P., & Kumar, R. (2019). Evaluation of electrochemical impedance and biocorrosion characteristics of as-cast and T4 heat treated AZ91 Mg-alloys in Ringer's solution. *Journal of Magnesium and Alloys*, *7*(1), 134-143.

[57] Bordbar-Khiabani, A., Ebrahimi, S., & Yarmand, B. (2020). In-vitro corrosion and bioactivity behavior of tailored calcium phosphate-containing zinc oxide coating prepared by plasma electrolytic oxidation. *Corrosion Science*, 108781.

[58] Poinern, G. E. J., Brundavanam, S., & Fawcett, D. (2012). Biomedical magnesium alloys: a review of material properties, surface modifications and potential as a biodegradable orthopaedic implant. *American Journal of Biomedical Engineering*, *2*(6), 218-240.

[59] Decup, M., Malec, D., & Bley, V. (2009). Impact of a surface laser treatment on the dielectric strength of α-alumina. *Journal of Applied Physics*, *106*(9), 094103.

[60] Dalla, P. T., Tragazikis, I. K., Exarchos, D. A., Dassios, K. G., Barkoula, N. M., & Matikas, T. E. (2019). Effect of carbon nanotubes on chloride penetration in cement mortars. *Applied Sciences*, *9*(5), 1032.

(Tables)

Table 1: Plasma electrolytic oxidation (PEO) treatment conditions and the properties of the resulted coatings obtained from MWCNT-containing electrolytes

Alloy/Application	**Electrolyte/ MWCNT characteristics**	**PEO conditions**	**Coating thickness and composition**	**Corrosion properties (i_{corr}, A/cm^2)**	**Dry wear properties**	**Tribocorrosion**	**Ref**
Al7075/Industrial	Na_2SiO_3, KOH, KF, MWCNT (150 mL/L) Average ∅ = 30 nm Average length: N/A	Current density: 150 mA/cm^2 Treatment time: 600 s	Thickness : N/A Composition : N/A MWCNT : Disclosed incorporation	MF : i_{corr} = 4.6×10^{-9} MC : i_{corr} = 8.33×10^{-10}	N/A	N/A	[27]
Al7075/Industrial	Na_2SiO_3 MWCNT (50 mL/L) Average ∅ = 35nm Average length: 10μm	Current density: 200 mA/cm^2 Treatment time: 900 s	Thickness : <10μm Composition : N/A MWCNT : Disclosed incorporation	MF : i_{corr} = 1.53×10^{8} MC : i_{corr} = 1.12×10^{-8}	N/A	N/A	[28]
Cp-Ti/Industrial	$Na_2Al_2O_4$,KOH, MWCNT (2 and 4 g/L) Average ∅ = 9.5nm Average length: 1.5μm	Bipolar square pulse Positive voltage: 300 – 375 V Negative Voltage: 60 – 75 V Treatment time: 5 min	Thickness: MF[1]-300= ~9μm MF[2]-375= ~13μm MC2-300= ~9μm MC2-375= ~12.5μm MC4-300= ~6μm MC4-375= ~11.5μm Composition: MF : Rutile MC2 and MC4= Rutile + Al_2TiO_5 MWCNT : Disclosed incorporation	N/A	N/A	N/A	[29]
Al6082/Industrial	$Na_2O{\cdot}Al_2O_3$, KOH, MWCNT Average ∅ 9.5nm Average length: 1.5μm	Bipolar square pulse Positive voltage: 400 Negative voltage: 80 Treatment time: 2, 5, and 10 min	Thickness: MF2= ~2μm MF5= ~13μm MF10= ~18μm MC2= ~4μm MC5= ~9μm MC10= ~14μm Composition: MF: γ-Al_2O_3 MC: γ-Al_2O_3 + α-Al_2O_3	N/A	MC shows better wear resistance.	N/A	[30]

[1] MF=MWCNTs-Free

[2] MC=MWCNTs-Containing

			MWCNT : Disclosed incorporation				
Commercially pure Al/Industrial	$Na_4P_2O_7$, $NaAlO_2$, KOH, functionalized-MWCNT (2 g/L) Average ∅ 25nm Average length: 1.5μm	520 V DC voltage Treatment time: 300 s	Thickness: MF: 29μm MC: 25μm Composition: MF and MC: γ-Al_2O_3 + α-Al_2O_3 + $AlPO_4$ MWCNT : Disclosed incorporation	N/A	N/A	N/A	[31]
Mg-AZ31/Industrial	Na_2SiO_3, KOH, KF, MWCNT (2.5, 5, and 10 g/L) Average ∅ N/A Average length: N/A	DC 10 A/dm^2 Treatment time: 600 s	Thickness: MF=19.3μm MC2.5=14.2μm MC5= 12.5μm MC10= 8μm Composition: MF and MC: MgO + Mg_2SiO_4 MWCNT : partially-oxidized	MF : $i_{corr} = 7.14\times10^{-9}$ MC2.5 : $i_{corr} = 3.67\times10^{-9}$ MC5 : $i_{corr} = 1.43\times10^{-9}$ MC10 : $i_{corr} = 4.8\times10^{-10}$	N/A	N/A	[32]

Table 2: Local EDS analyses of PEO and PCT coatings formed on AZ31B Mg alloy.

Specimens	Mg	O	Al	Si	P	Ca	C
PEO	23.31	50.96	1.01	8.68	2.25	0.12	10.80
PCT	22.01	48.23	0.96	6.27	0.5	0.12	21.21

Table 3: Electrochemical parameters obtained from Tafel plots.

Specimens	i_{corr} (A/cm^2)	E_{corr} (V)	E_{bd} (V)
BM0.5	1.8×10^{-6}	-1.44	-1.44
BM50	6.74×10^{-7}	-1.34	-1.34
PEO0.5	7.6×10^{-9}	-1.47	-1.44
PEO50	8.74×10^{-7}	-1.3	-1.3
PCT0.5	9.23×10^{-9}	-1.5	-1.42
PCT50	7.79×10^{-8}	-1.52	-1.32

Figure Captions

Figure 1: TEM images of pristine MWCNTs used in current work.

Figure 2: Schematic of experimental setup for tribocorrosion assessments.

Figure 3: Schematic of experimental setup for electrochemical measurements.

Figure 4: Rms current/voltage-time transients during the different MAO processes.

Figure 5: Color comparison between PCT and PEO coatings (a and b). Optical profilometry images of PEO ((c) and (d)) and PCT ((e) and (f)) coatings.

Figure 6: The surface SEM micrographs of PEO (a) and PCT (b) coatings and the cross-sectional SEM micrographs of PEO (c) and PCT (d) coatings.

Figure 7: The surface FE-SEM micrographs of PEO (a) and PCT (b) coatings.

Figure 8: The Raman spectra of MWCNTs powder, PEO and PCT coatings.

Figure 9: (a) XRD patterns for PEO and PCT coatings (10^{o}-90^{o}). (b) XRD pattern for PCT coating (10^{o}-60^{o}).

Figure 10: Dynamic data of Coefficient of Friction (COF) as a function of sliding distance for BM, PEO and PCT coatings.

Figure 11: (a, c and e) Optical image of wear track corresponded to BM, PEO coating and PCT coating. (b, d and f) 2D Wear track profiles corresponded to BM, PEO coating and PCT coating. (g) Wear track depths on BM, PEO and PCT coatings after dry wear and tribocorrosion tests.

Figure 12: Variation of OCP values for BM, PEO and PCT coatings.

Figure 13: (a), (c) and (e): SEM micrographs of the wear tracks of BM, PEO and PCT coatings after tribocorrosion tests. (b), (d) and (f): Bar graphs of extracted information from EDS spectra taken from inside and outside of wear grooves corresponded to BM, PEO and PCT coatings.

Figure 14: Potentiodynamic polarization results of BM, PEO and PCT coatings after 0.5 h and 50 h immersion in the quasi-in vivo environment.

Figure 15: The Raman spectra taken from inside of a pore.

Figures

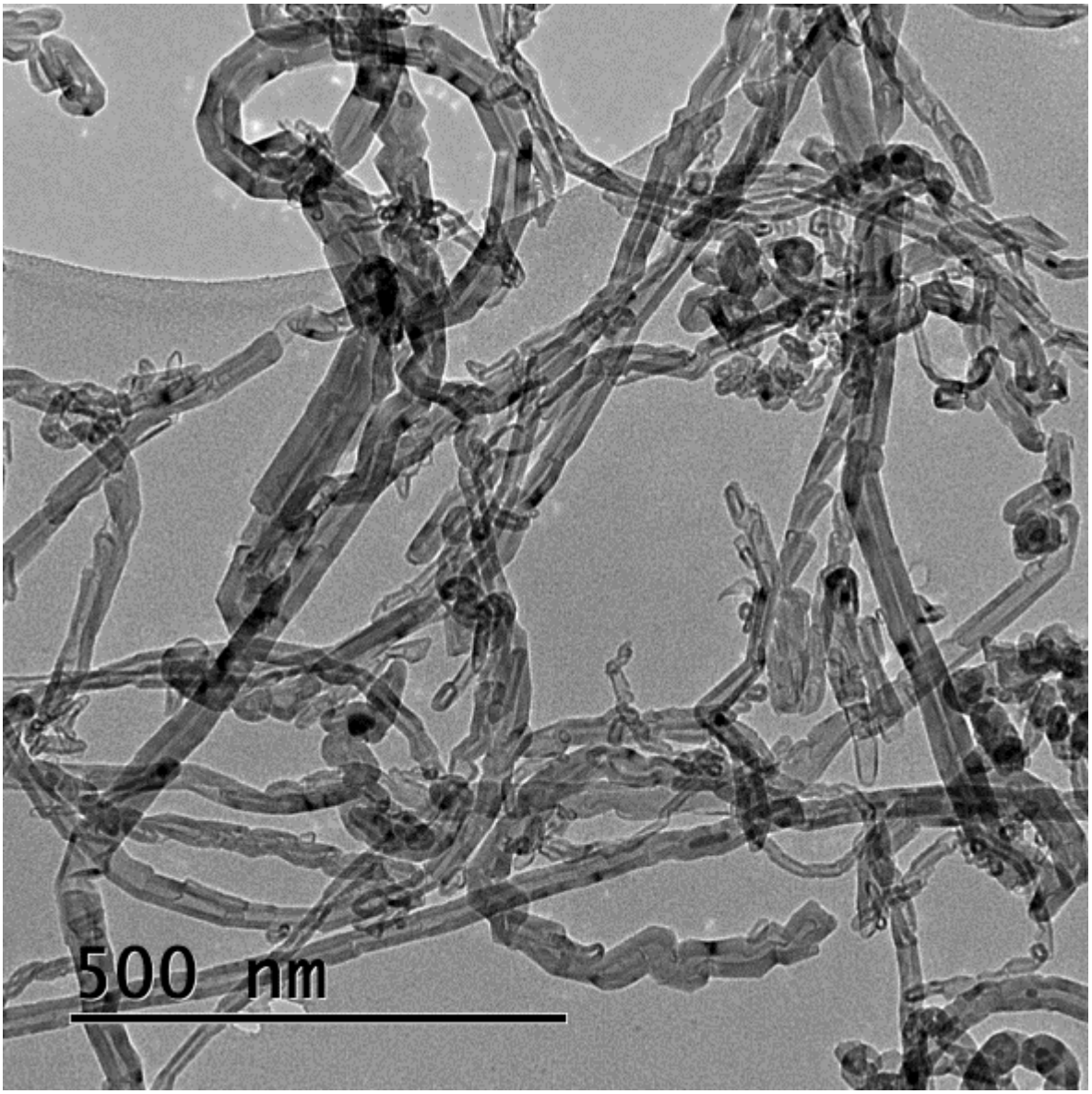

Figure 1

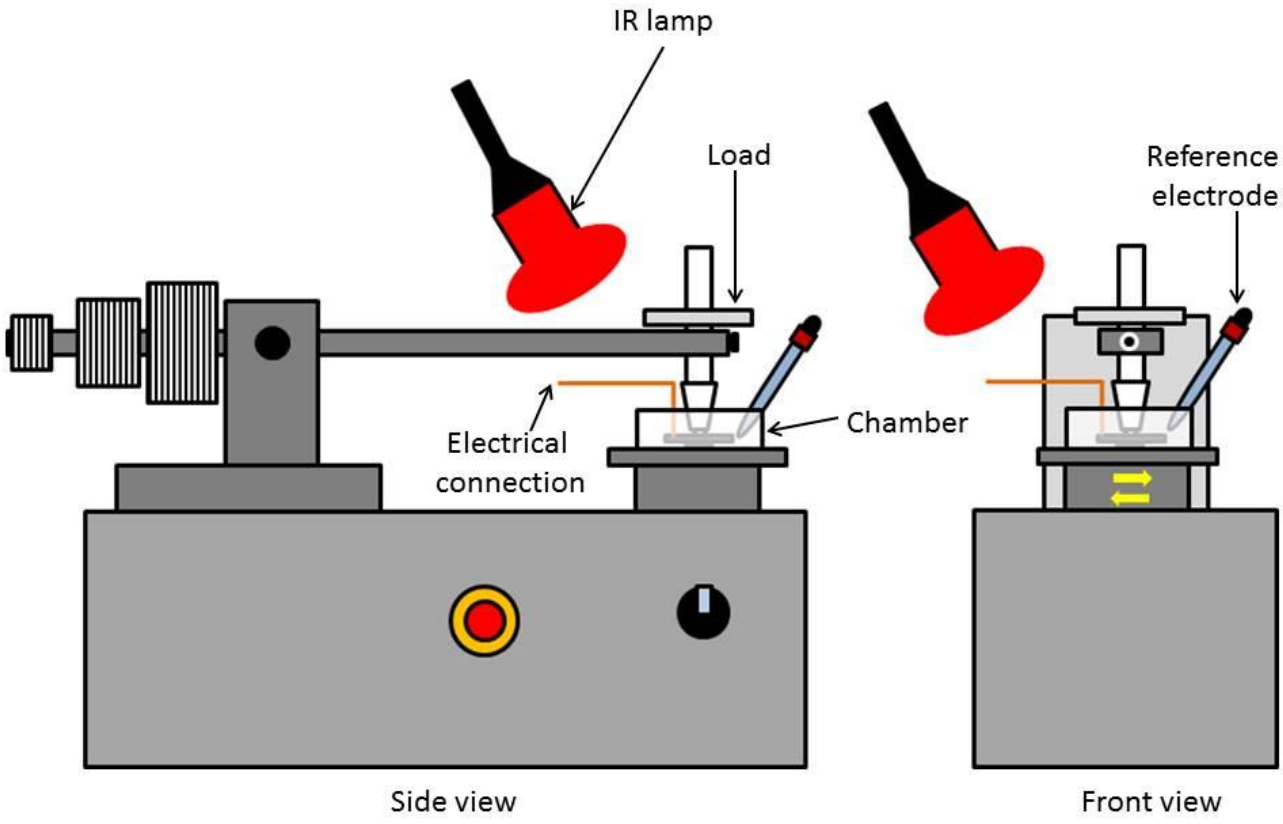
IR lamp
Load
Reference electrode
Electrical connection
Chamber
Side view
Front view

Figure 2

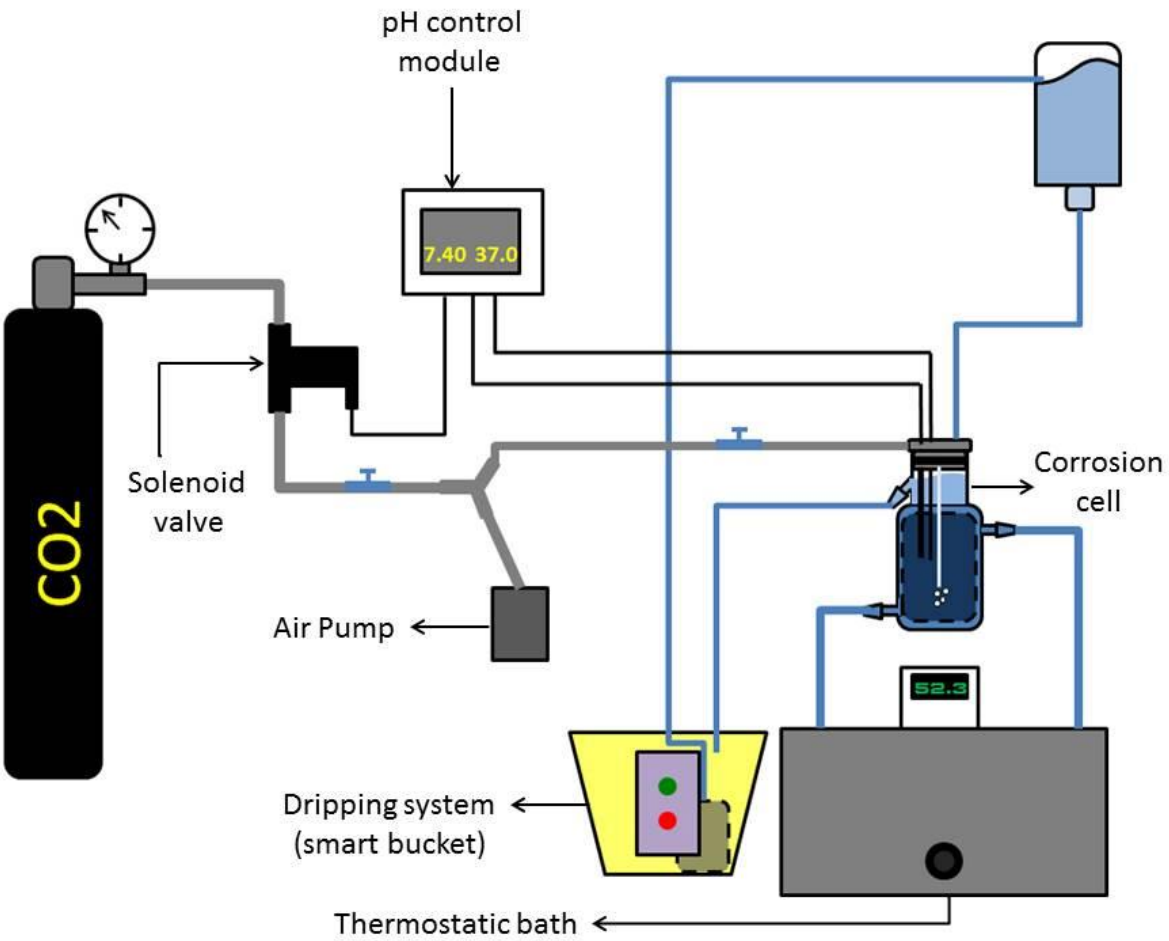
pH control
module
7.40 37.0
CO2
Solenoid
valve
Air Pump
Corrosion
cell
52.3
Dripping system
(smart bucket)
Thermostatic bath

Figure 3

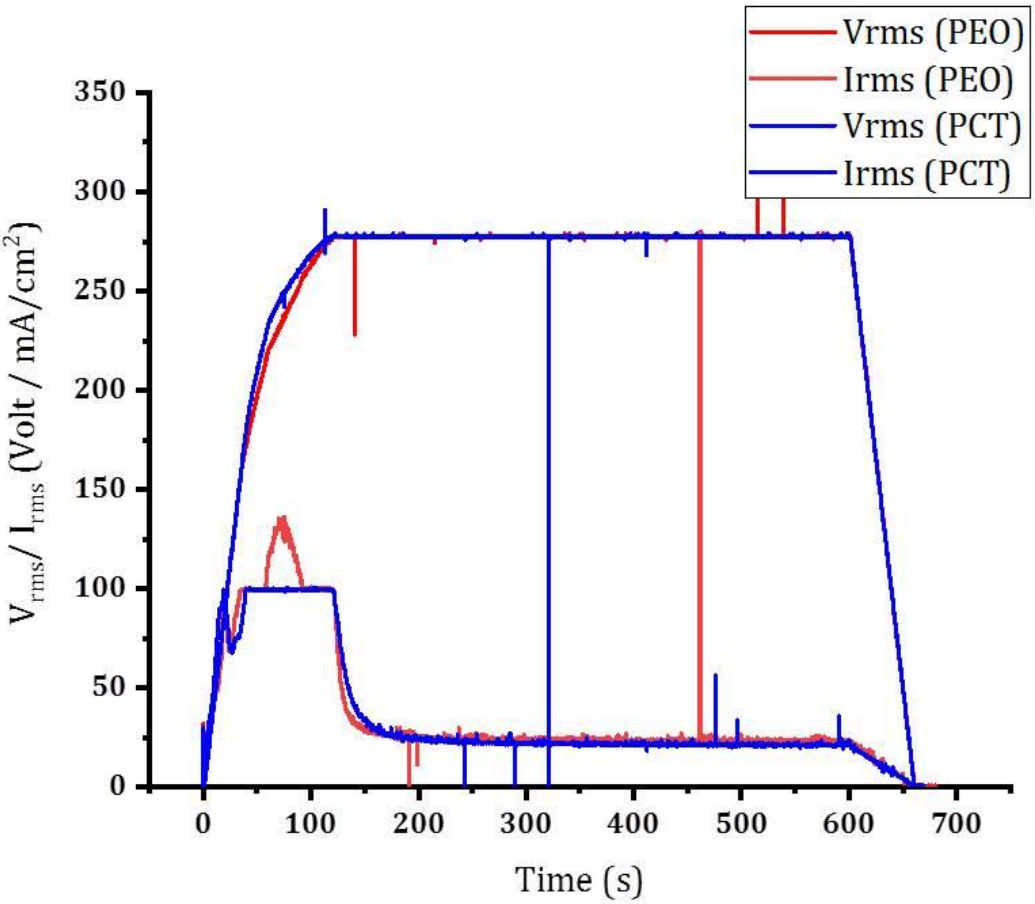
Vrms (PEO)
Irms (PEO)
Vrms (PCT)
Irms (PCT)
350
300
250
200
150
100
50
0
V_{rms}/ I_{rms} (Volt / mA/cm^2)
0
100
200
300
400
500
600
700
Time (s)

Figure 4

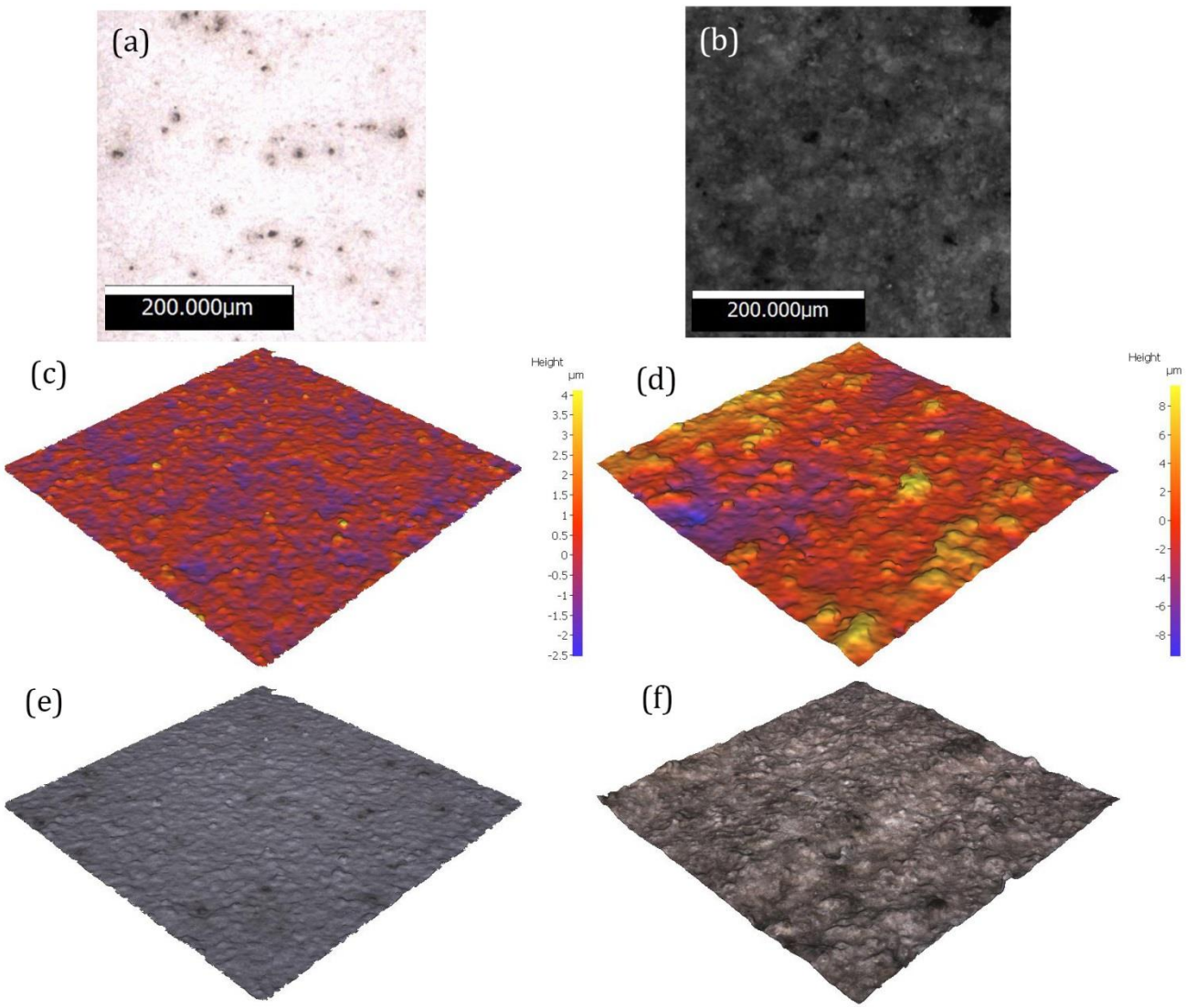
(a)
200.000µm
(b)
200.000µm
(c)
Height
µm
4
3.5
3
2.5
2
1.5
1
0.5
0
-0.5
-1
-1.5
-2
-2.5
(d)
Height
µm
8
6
4
2
0
-2
-4
-6
-8
(e)
(f)

Figure 5

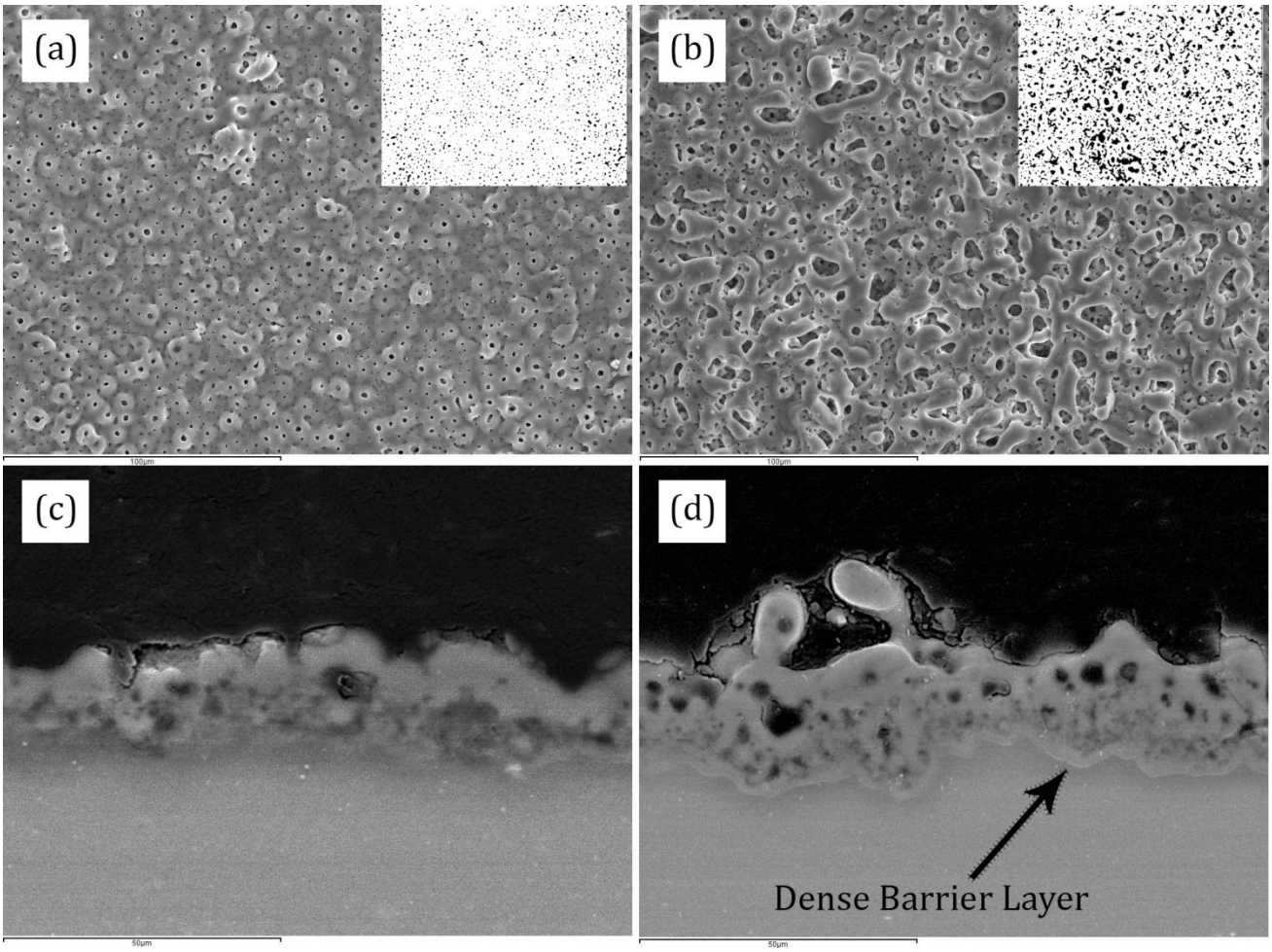

Figure 6

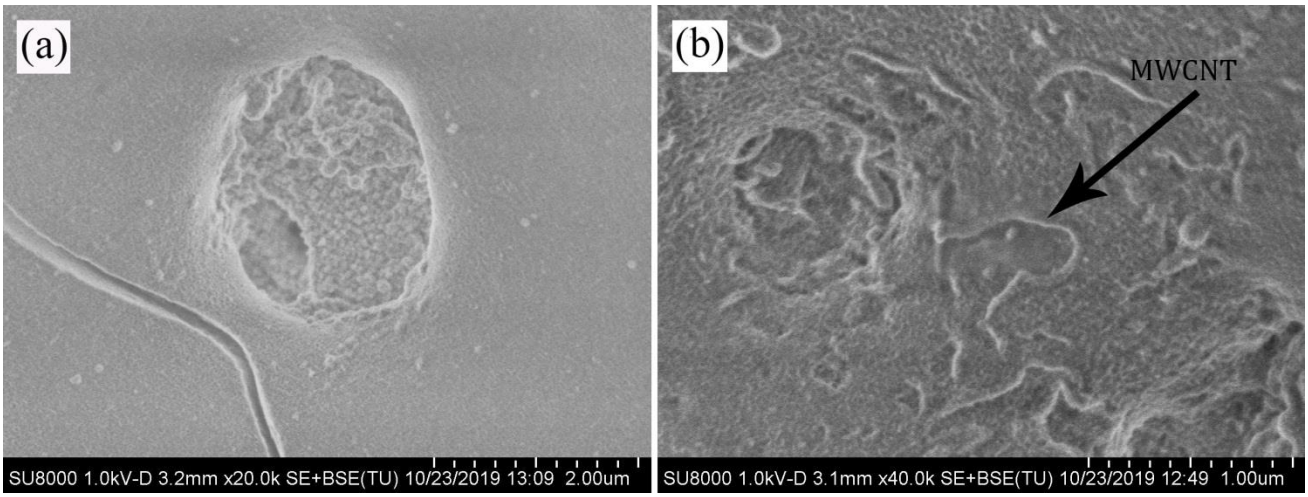
(a)
SU8000 1.0kV-D 3.2mm x20.0k SE+BSE(TU) 10/23/2019 13:09 2.00um
(b)
MWCNT
SU8000 1.0kV-D 3.1mm x40.0k SE+BSE(TU) 10/23/2019 12:49 1.00um

Figure 7

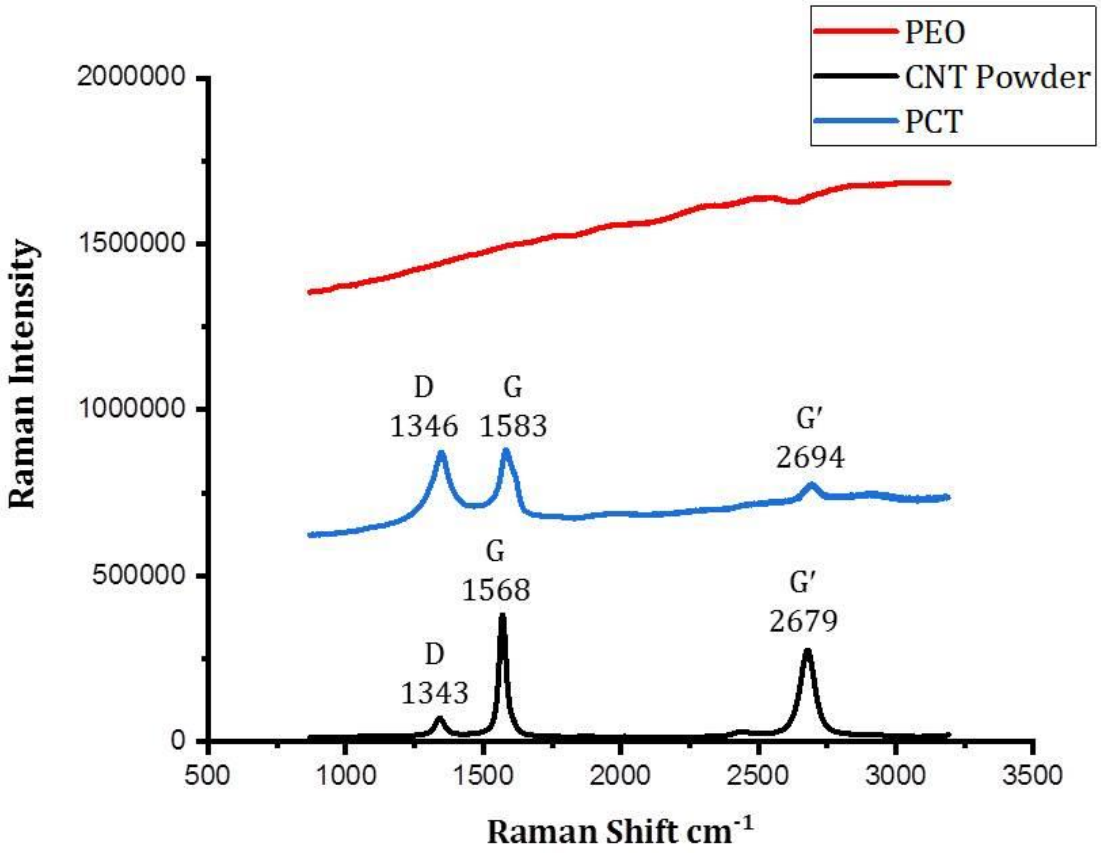
PEO
CNT Powder
PCT
Raman Intensity
2000000
1500000
1000000
500000
0
D
1346
G
1583
G′
2694
G
1568
D
1343
G′
2679
500
1000
1500
2000
2500
3000
3500
Raman Shift cm-1

Figure 8

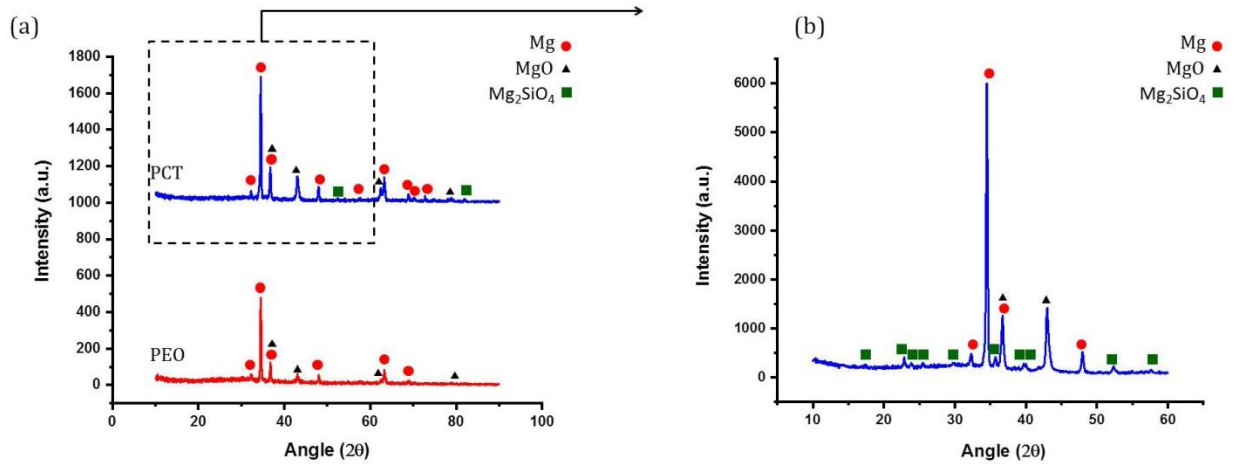
(a)
Mg
MgO
Mg2SiO4
PCT
PEO
Intensity (a.u.)
Angle (2θ)
(b)
Mg
MgO
Mg2SiO4
Intensity (a.u.)
Angle (2θ)

Figure 9

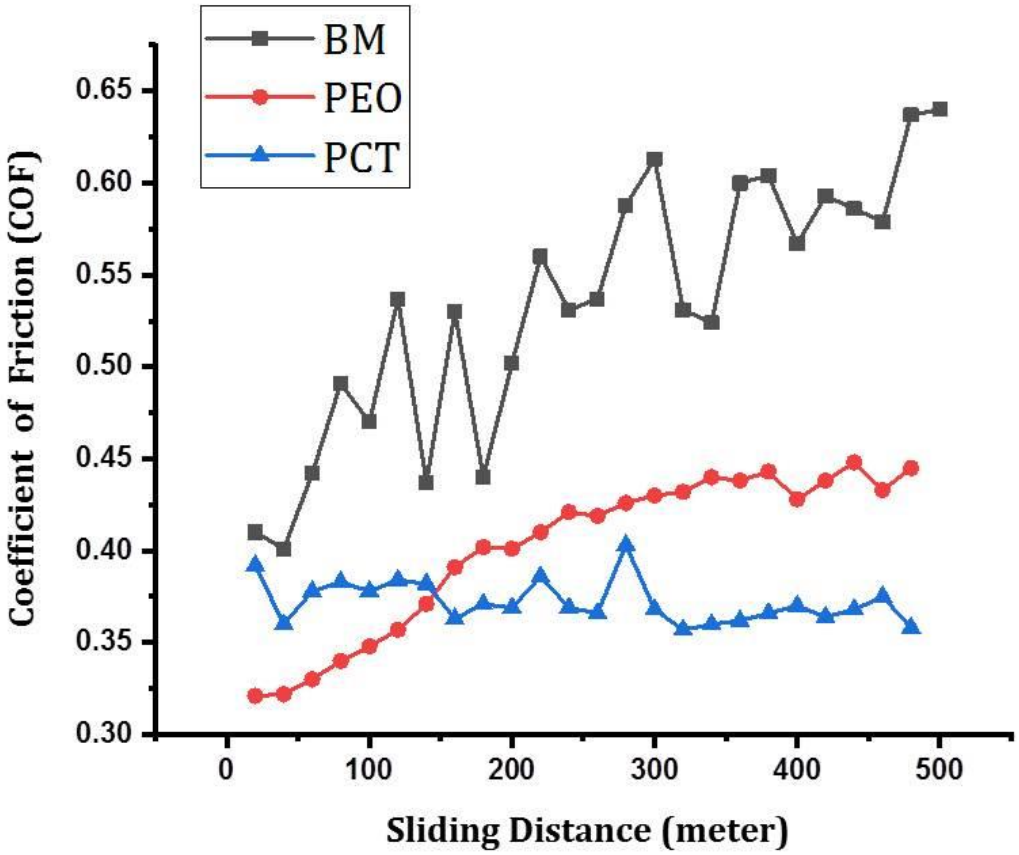
BM
PEO
PCT
Coefficient of Friction (COF)
0.65
0.60
0.55
0.50
0.45
0.40
0.35
0.30
0
100
200
300
400
500
Sliding Distance (meter)

Figure 10

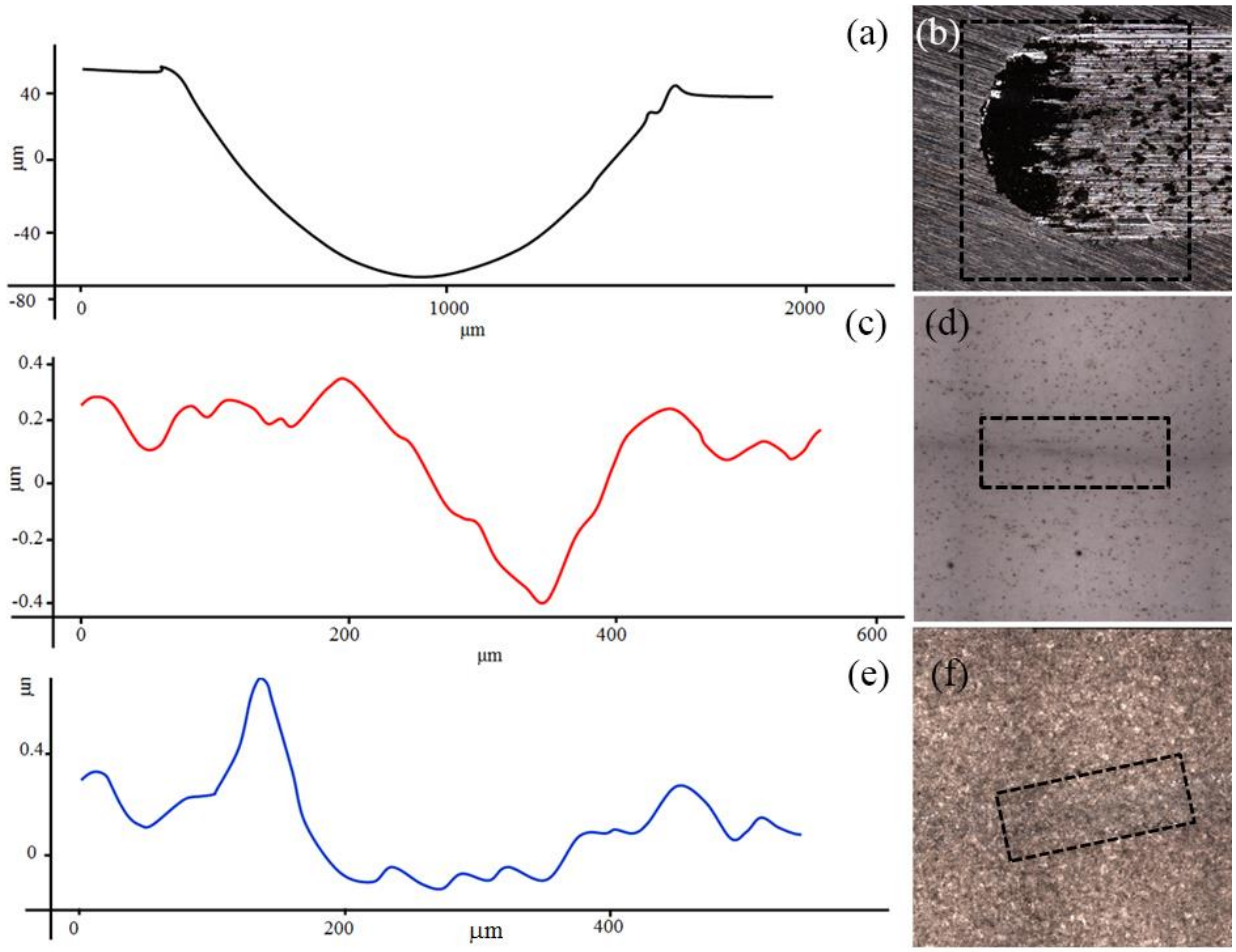
(a)
(b)
(c)
(d)
(e)
(f)
µm
40
0
-40
-80
0
1000
2000
0.4
0.2
-0.2
-0.4
200
400
600

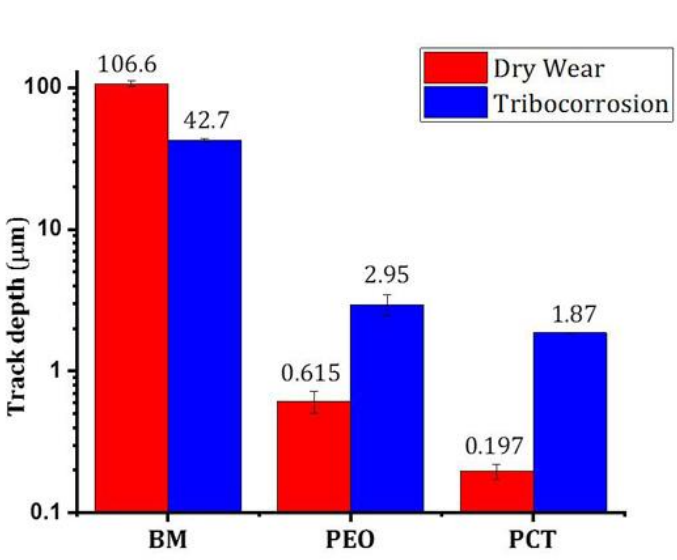
(g)
Dry Wear
Tribocorrosion
Track depth (µm)
106.6
42.7
2.95
0.615
1.87
0.197
100
10
1
0.1
BM
PEO
PCT

Figure 11

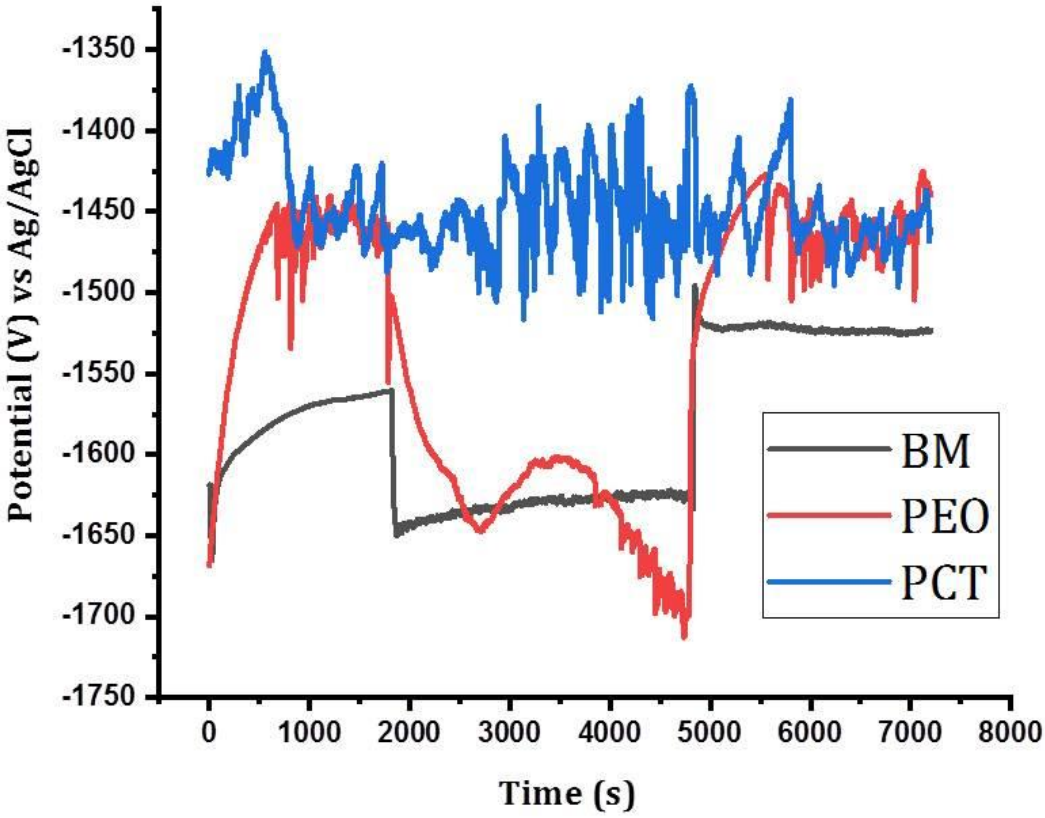
Potential (V) vs Ag/AgCl
-1350
-1400
-1450
-1500
-1550
-1600
-1650
-1700
-1750
0
1000
2000
3000
4000
5000
6000
7000
8000
Time (s)
BM
PEO
PCT

Figure 12

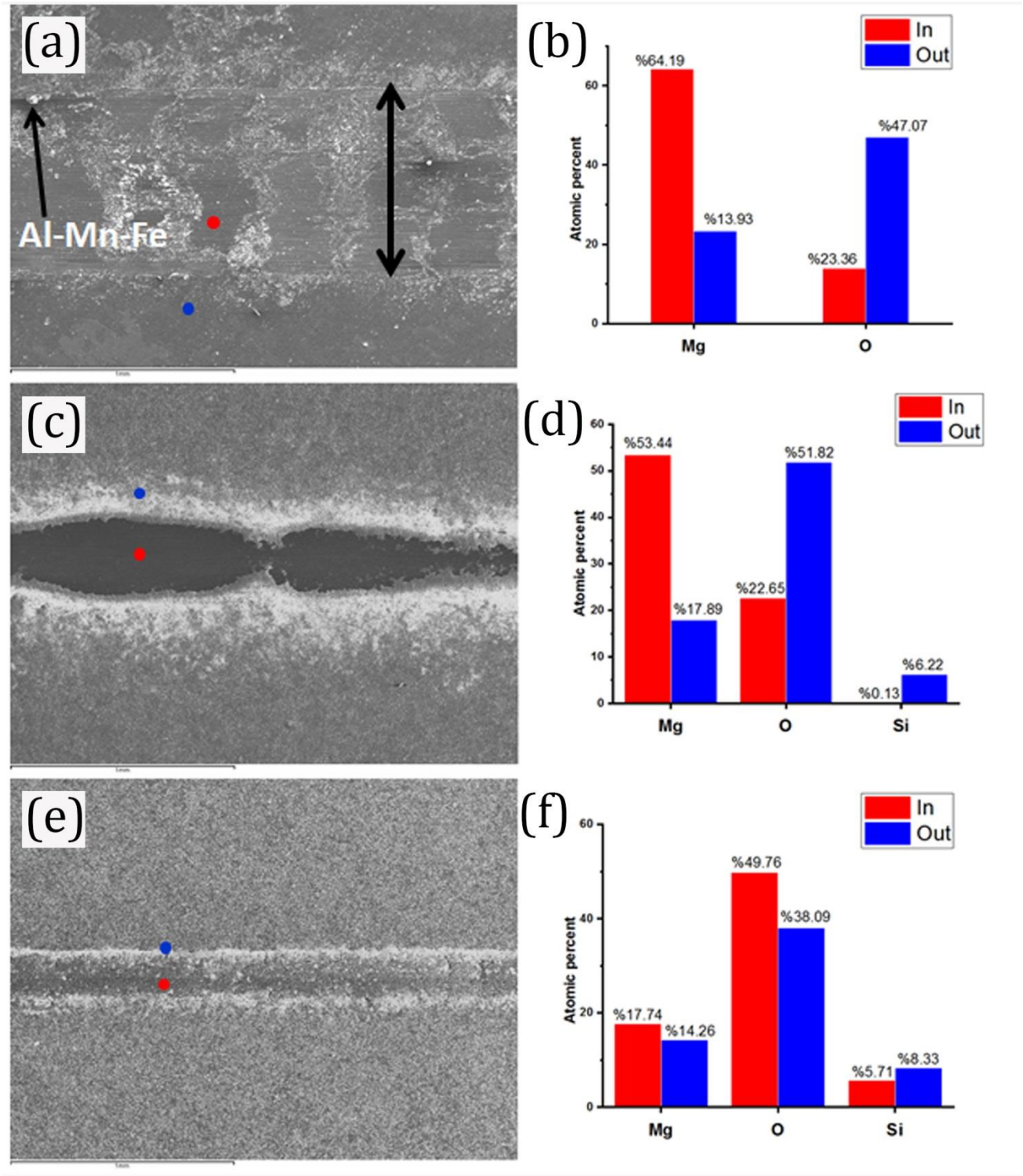
(a)
Al-Mn-Fe
(b)
In
Out
%64.19
%13.93
%23.36
%47.07
Atomic percent
Mg
O
(c)
(d)
%53.44
%17.89
%22.65
%51.82
%0.13
%6.22
Mg
O
Si
(e)
(f)
%17.74
%14.26
%49.76
%38.09
%5.71
%8.33

Figure 13

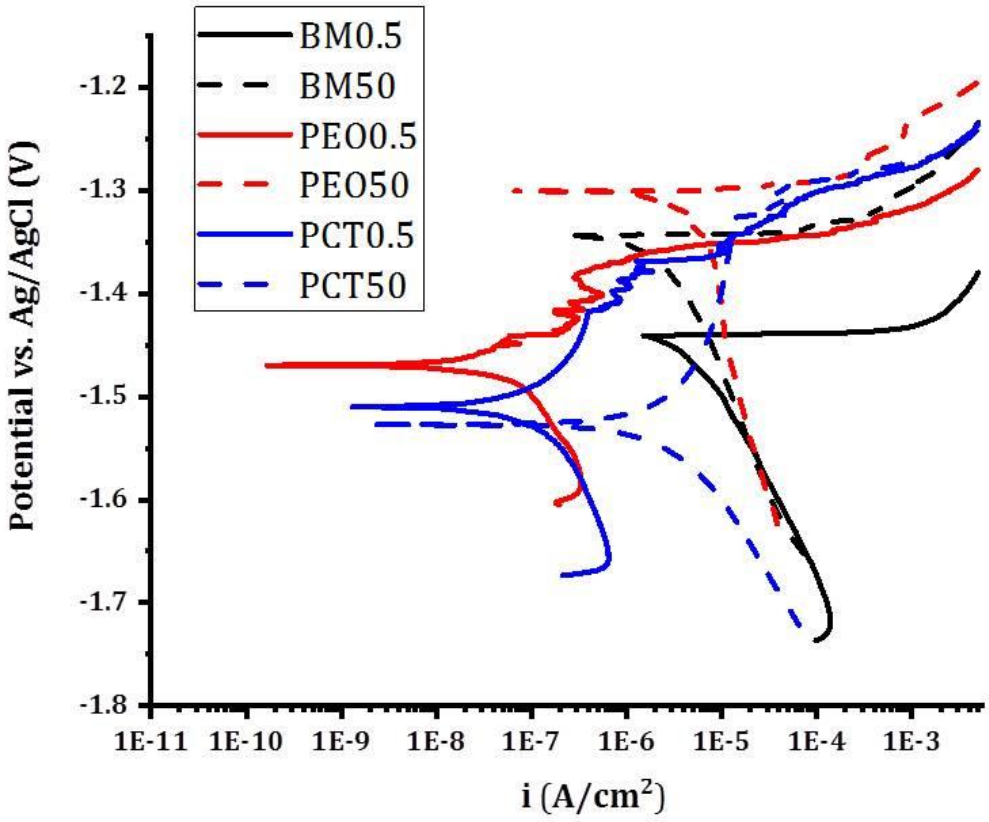
BM0.5
BM50
PEO0.5
PEO50
PCT0.5
PCT50
Potential vs. Ag/AgCl (V)
-1.2
-1.3
-1.4
-1.5
-1.6
-1.7
-1.8
1E-11
1E-10
1E-9
1E-8
1E-7
1E-6
1E-5
1E-4
1E-3
i (A/cm²)

Figure 14

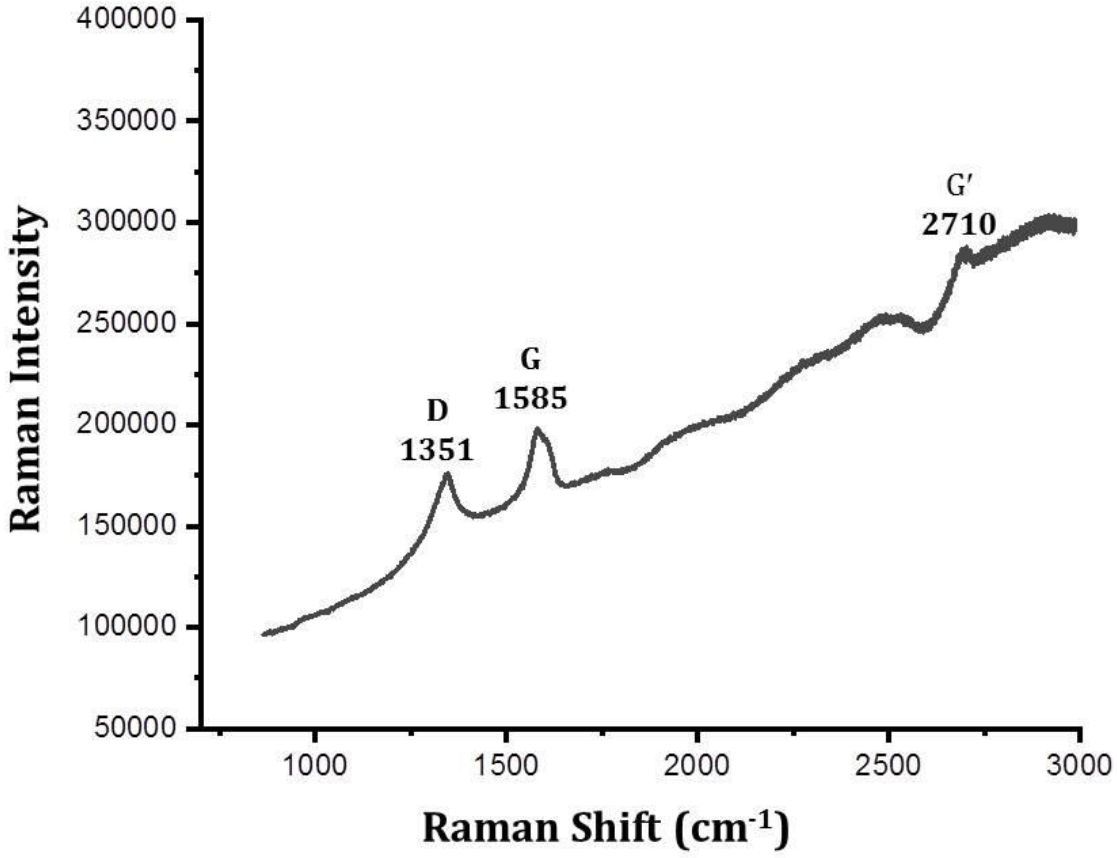
Raman Intensity
400000
350000
300000
250000
200000
150000
100000
50000
1000
1500
2000
2500
3000
Raman Shift (cm-1)
D
1351
G
1585
G′
2710

Figure 15

Declaration of interests

☒ The authors declare that they have no known competing financial interests or personal relationships that could have appeared to influence the work reported in this paper.

☐The authors declare the following financial interests/personal relationships which may be considered as potential competing interests:

CRediT author statement

Manuscript title: Biotribology and biocorrosion of MWCNTs-reinforced PEO coating on AZ31B Mg alloy

All persons who meet authorship criteria are listed as authors, and all authors certify that they have participated sufficiently in the work to take public responsibility for content, including participation in Conceptualization, Methodology, Software, Validation, Formal analysis, Investigation, Resources, Data Curation, Writing - Original Draft, Writing - Review & Editing, Visualization, Supervision, Project administration, Funding acquisition or revision of the manuscript.

Author contributions

Morteza Daavari: Investigation, Conceptualization, Methodology, Data Curation, Visualization, Writing - Original Draft.

Masoud Atapour*:* Funding acquisition, Conceptualization, Resources, Validation, Supervision, Formal analysis, Writing - Original Draft , Writing - Review & Editing.

Marta Mohedano*:* Funding acquisition, Resources, Investigation, Formal Analysis.

Raul Arrabal: Conceptualization, Resources, Supervision, Investigation, Formal Analysis, Validation, Writing - Review & Editing.

Endzhe Matykina: Conceptualization, Resources, Supervision, Investigation, Formal Analysis, Data Curation, Validation, Writing - Review & Editing.

Aboozar Taherizadeh*:* Resources, Writing - Review & Editing, Supervision.